J. Mech. Phys. Solids 149 (2021) 104296

Contents lists available at ScienceDirect

Journal of the Mechanics and Physics of Solids

journal homepage: www.elsevier.com/locate/jmps

Buckling of thermalized elastic sheets

Ali Morshedifard [a,1], Miguel Ruiz-García [b,c,1], Mohammad Javad Abdolhosseini Qomi [a,*], Andrej Košmrlj [d,e,*]

[a] Department of Civil and Environmental Engineering, Henry Samueli School of Engineering, E4130 Engineering Gateway, University of California, Irvine, Irvine, CA 92697-2175, USA
[b] Department of Physics and Astronomy, University of Pennsylvania, Philadelphia, PA 19104, USA
[c] Department of Applied Mathematics, ETSII, Universidad Politécnica de Madrid, Madrid 28006, Spain
[d] Department of Mechanical and Aerospace Engineering, Princeton University, Princeton, NJ 08544, USA
[e] Princeton Institute for the Science and Technology of Materials, Princeton University, Princeton, NJ 08544, USA

ARTICLE INFO

Keywords:
Buckling
Plates
Thermomechanical process
Elastic material

ABSTRACT

Steady progress in the miniaturization of structures and devices has reached a scale where thermal fluctuations become relevant and it is thus important to understand how such fluctuations affect their mechanical stability. Here, we investigate the buckling of thermalized square sheets under either compression or shear. We demonstrate that thermal fluctuations increase the critical buckling load compared to the classical Euler buckling load due to the enhanced scale-dependent bending rigidity for sheets that are much larger than a characteristic thermal length scale. The presented results are universal and apply to a wide range of microscopic sheets. These results are especially relevant for atomically thin 2D materials, where thermal fluctuations can significantly increase the critical buckling load because the thermal length scale is on the order of nanometers at room temperature.

1. Introduction

The mechanics of slender structures has been studied for centuries (Timoshenko, 1953) but is still actively explored to this day because geometrical nonlinearities lead to many interesting phenomena involving buckling, wrinkling, and folding (Brau et al., 2013; Chopin and Kudrolli, 2013; Stoop et al., 2015; Paulsen et al., 2016; Nagashima et al., 2017). In the 19th century, a concentrated effort was made to characterize critical loads at the onset of mechanical instabilities (Timoshenko and Woinowsky-Krieger, 1959; van der Heijden, 2009; Novozhilov, 1959; Ciarlet, 2000; Landau and Lifshitz, 1970), because engineers had to design stable and safe structures and machines. However, in recent years, it has become a trend to exploit these instabilities in order to make so-called mechanical metamaterials (Bertoldi et al., 2017; Kadic et al., 2019).

Many slender structures and mechanical metamaterials have been successfully translated from the macroscopic to the microscopic scale (Blees et al., 2015; Zhang et al., 2015; Leong et al., 2015; Malachowski et al., 2014; Xu et al., 2017; Miskin et al., 2018; Reynolds et al., 2019). As we strive to make devices and machines smaller and smaller, we are ultimately going to reach a scale where defects and thermal fluctuations become relevant. Thus, it is important to characterize how these two effects are going to affect the mechanical properties and the stability of slender structures. In this work, we focus on thermal fluctuations that become relevant once the narrow dimensions of structures reach the scale of nanometers. In many systems this condition is already satisfied, such as for graphene kirigami (Blees et al., 2015) and graphene-based self-folding origami (Xu et al., 2017; Miskin et al., 2018),

* Corresponding authors.
E-mail addresses: mjaq@uci.edu (M.J. Abdolhosseini Qomi), andrej@princeton.edu (A. Košmrlj).
[1] These two authors contributed equally.

https://doi.org/10.1016/j.jmps.2021.104296
Received 26 July 2020; Received in revised form 13 December 2020; Accepted 6 January 2021
Available online 15 January 2021

where we expect that thermal fluctuations significantly affect their mechanical properties, including the critical buckling load, which is the focus of this work.

Here, we consider a coarse-grained description of a freely suspended linear elastic sheet with the bending rigidity κ_0, the Gauss bending rigidity κ_{G0} and the 2D Lamé constants λ_0 and μ_0, where the 2D Young's modulus is $Y_0 = 4\mu_0(\mu_0+\lambda_0)/(2\mu_0+\lambda_0)$ and the Poisson's ratio $\nu_0 = \lambda_0/(2\mu_0+\lambda_0)$. The free energy cost associated with small deformations of sheets around the reference flat state is (Landau and Lifshitz, 1970)

$$E = \int dxdy\ \frac{1}{2}\left[\lambda_0 u_{ii}^2 + 2\mu_0 u_{ij}^2 + \kappa_0 K_{ii}^2 - 2\kappa_{G0}\det(K_{ij})\right] - \oint ds\, t_i u_i, \tag{1}$$

where summation over all indices $i,j \in \{x,y\}$ is implied. The first two terms describe the cost of stretching, shearing and compressing, and the next two terms the cost of bending. The boundary integral measures the work done by external tractions $t_i = \sigma_{ij} m_j$, where σ_{ij} describes the stress tensor of external loads and m_i is the unit normal vector in the X–Y plane to the sheet boundary. The strain tensors

$$\begin{aligned} u_{ij} &= \frac{1}{2}(\partial_i u_j + \partial_j u_i) + \frac{1}{2}(\partial_i h)(\partial_j h), \\ K_{ij} &= \partial_i \partial_j h, \end{aligned} \tag{2}$$

describe deformations from the preferred flat metric and zero curvature respectively. We kept only the lowest orders in terms of the in-plane displacements $u_i(\mathbf{r})$ and out-of-plane displacements $h(\mathbf{r})$ with $\mathbf{r} \equiv (x,y)$, which is known as the Föppl–von Kármán approximation (Landau and Lifshitz, 1970). The effects of thermal fluctuations are reflected in correlation functions obtained from functional integrals (Nelson et al., 2004; Katsnelson, 2012),

$$\begin{aligned} G_{hh}(\mathbf{r}_2-\mathbf{r}_1) &\equiv \langle h(\mathbf{r}_2)h(\mathbf{r}_1)\rangle = \frac{1}{Z}\int \mathcal{D}[u_i(\mathbf{r}),h(\mathbf{r})]\ h(\mathbf{r}_2)h(\mathbf{r}_1)e^{-E[u_i(\mathbf{r}),h(\mathbf{r})]/k_BT}, \\ G_{u_iu_j}(\mathbf{r}_2-\mathbf{r}_1) &\equiv \langle u_i(\mathbf{r}_2)u_j(\mathbf{r}_1)\rangle = \frac{1}{Z}\int \mathcal{D}[u_k(\mathbf{r}),h(\mathbf{r})]\ u_i(\mathbf{r}_2)u_j(\mathbf{r}_1)e^{-E[u_k(\mathbf{r}),h(\mathbf{r})]/k_BT}, \end{aligned} \tag{3}$$

where k_B is the Boltzmann constant, T the ambient temperature, and $Z = \int \mathcal{D}[u_i(\mathbf{r}),h(\mathbf{r})]e^{-E[u_i(\mathbf{r}),h(\mathbf{r})]/k_BT}$ the partition function. Before discussing the buckling of sheets, we briefly comment on the thermally fluctuating sheets in the absence of external loads ($\sigma_{ij} \equiv 0$) to introduce the relevant terminology.

2. Freely suspended fluctuating sheets

For freely suspended sheets without external loads, thermal fluctuations effectively modify elastic constants and make them scale dependent. We refer to these effective constants as the renormalized elastic constants, which can be extracted from the fluctuation spectra as (Nelson et al., 2004; Katsnelson, 2012; Amorim et al., 2016; Košmrlj and Nelson, 2016; Ahmadpoor et al., 2017)

$$\begin{aligned} G_{hh}(\mathbf{q}) &\equiv \langle h(\mathbf{q})h(-\mathbf{q})\rangle = \frac{k_BT}{A_0\kappa_R(q)q^4}, \\ G_{u_iu_j}(\mathbf{q}) &\equiv \langle u_i(\mathbf{q})u_j(-\mathbf{q})\rangle = \frac{k_BTP_{ij}^T(\mathbf{q})}{A_0\mu_R(q)q^2} + \frac{k_BTP_{ij}^L(\mathbf{q})}{A_0\left(2\mu_R(q)+\lambda_R(q)\right)q^2}, \end{aligned} \tag{4}$$

where A_0 is the undeformed area of the sheet, $\mathbf{q} \equiv (q_x,q_y)$, $q = |\mathbf{q}|$, and the Fourier transform is defined as $f(\mathbf{q}) \equiv \int (d^2\mathbf{r}/A_0)\, e^{-i\mathbf{q}\cdot\mathbf{r}} f(\mathbf{r})$. For the in-plane fluctuations $G_{u_iu_j}(\mathbf{q})$ the two terms describe the spectra of transverse and longitudinal phonons, where $P_{ij}^T(\mathbf{q}) = \delta_{ij} - q_iq_j/q^2$ and $P_{ij}^L(\mathbf{q}) = q_iq_j/q^2$ are the transverse and longitudinal projection operators, respectively. The correlation functions in Eq. (4) are plotted in Fig. 1(a–c).

Thermal fluctuations effectively increase the bending rigidity and reduce the 2D Lamé constants and 2D Young's modulus, which scale as

$$\begin{aligned} \frac{\kappa_R(q)}{\kappa_0} &\sim \begin{cases} 1, & q \gg q_{\text{th}} \\ (q/q_{\text{th}})^{-\eta}, & q \ll q_{\text{th}} \end{cases}, \\ \frac{\lambda_R(q)}{\lambda_0}, \frac{\mu_R(q)}{\mu_0}, \frac{Y_R(q)}{Y_0} &\sim \begin{cases} 1, & q \gg q_{\text{th}} \\ (q/q_{\text{th}})^{+\eta_u}, & q \ll q_{\text{th}} \end{cases}. \\ \nu_R(q) &\sim \begin{cases} \nu_0, & q \gg q_{\text{th}} \\ -\frac{1}{3}, & q \ll q_{\text{th}} \end{cases}, \end{aligned} \tag{5}$$

where the renormalized Young's modulus $Y_R(q)$ and the renormalized Poisson' s ratio $\nu_R(q)$ are defined as $Y_R(q) = 4\mu_R(q)[\mu_R(q)+\lambda_R(q)]/[2\mu_R(q)+\lambda_R(q)]$ and $\nu_R(q) = \lambda_R(q)/[2\mu_R(q)+\lambda_R(q)]$, respectively. The scaling exponents $\eta \approx 0.80$–0.85 and $\eta_u = 2-2\eta \approx 0.3$–$0.4$, were estimated theoretically (Nelson and Peliti, 1987; Aronovitz and Lubensky, 1988; Guitter et al., 1988, 1989; Nelson and Radzihovsky, 1991; Aronovitz et al., 1989; Le Doussal and Radzihovsky, 1992; Kownacki and Mouhanna, 2009; Coquand et al., 2020) and confirmed in atomistic and coarse-grained Monte Carlo simulations (Zhang et al., 1993; Bowick et al., 1996, 1997; Los et al., 2009; Roldan et al., 2011; Tröster, 2013, 2015; Los et al., 2016). These exponents quantify the scale dependence of the elastic

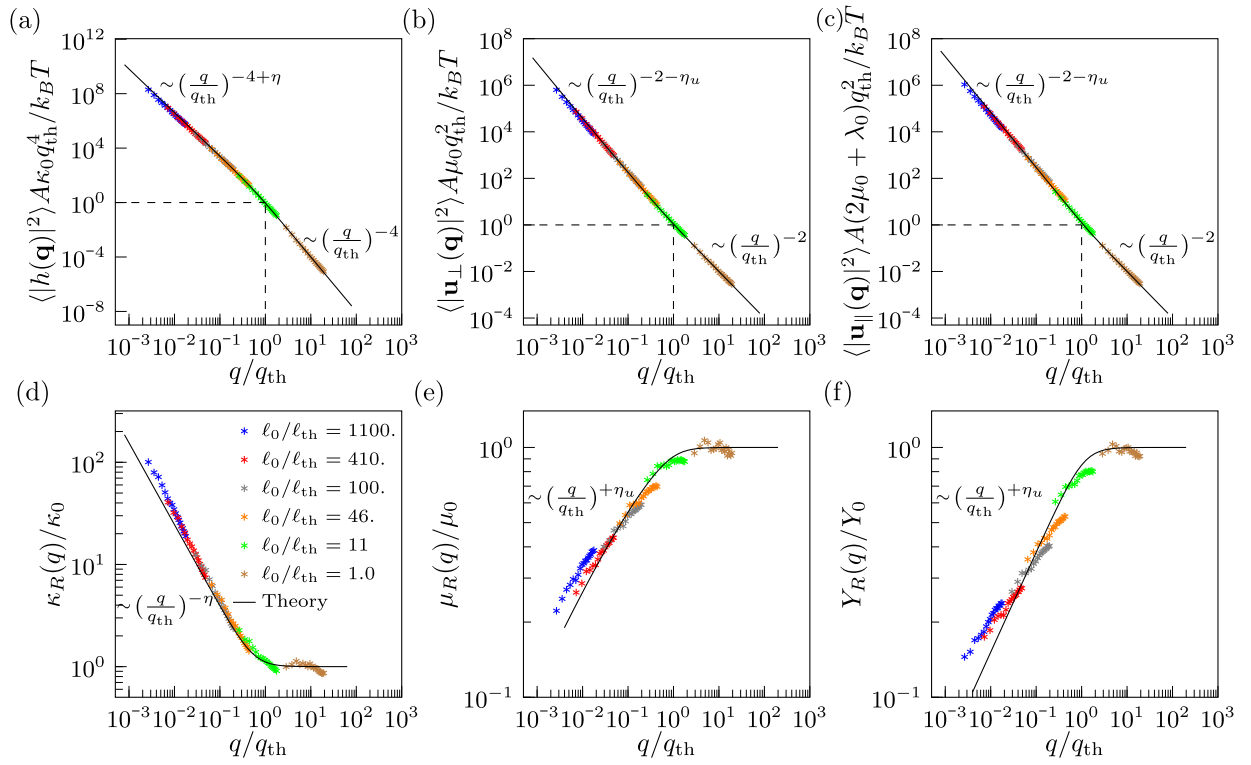

Fig. 1. Correlation functions for (a) height fluctuations $h(\mathbf{q})$, (b) transverse in-plane phonons $u_{\perp i}(\mathbf{q}) = P^T_{ij}u_i(\mathbf{q})$, and (c) longitudinal in-plane phonons $u_{\parallel i}(\mathbf{q}) = P^L_{ij}u_i(\mathbf{q})$. Correlation functions are used to extract the renormalized elastic constants: (d) the renormalized bending rigidity $\kappa_R(q) = (k_BT/A_0q^4)\langle|h(\mathbf{q})|^2\rangle^{-1}$, (e) the renormalized shear modulus $\mu_R(q) = (k_BT/A_0q^2)\langle|\mathbf{u}_\perp(\mathbf{q})|^2\rangle^{-1}$, and (f) the renormalized Young's modulus $Y_R(q) = 4(k_BT/A_0q^2)\langle|\mathbf{u}_\perp(\mathbf{q})|^2\rangle^{-1}\left[\langle|\mathbf{u}_\parallel(\mathbf{q})|^2\rangle^{-1} - \langle|\mathbf{u}_\perp(\mathbf{q})|^2\rangle^{-1}\right]/\langle|\mathbf{u}_\parallel(\mathbf{q})|^2\rangle^{-1}$. Correlation functions and renormalized elastic constants are normalized by the zero temperature elastic constants values (κ_0, μ_0, λ_0, Y_0), the undeformed sheet area A_0, the ambient temperature T, and the Boltzmann constant k_B. The temperature dependent transition wave vector $q_{\rm th}$ and the corresponding thermal lengthscale $\ell_{\rm th} = 2\pi/q_{\rm th}$ are defined in Eqs. (6) and (7). Black solid lines correspond to the theoretical estimates that were obtained with the perturbative renormalization group procedure (Košmrlj and Nelson, 2016). Data with colored symbols was obtained from molecular dynamic simulations of nearly square sheets with the undeformed size ℓ_0 that are described in Section 3.1. For simulation data, the correlation functions for different wavevectors $\mathbf{q}$ were binned into annular bins of width $\Delta q = 2\pi/\ell_0$.

constants driven by thermal fluctuations in the range of wave vectors up to the transition scale (Aronovitz and Lubensky, 1988; Guitter et al., 1988, 1989; Nelson and Radzihovsky, 1991)

$$q_{\rm th} = \sqrt{\frac{3k_BTY_0}{16\pi\kappa_0^2}} \tag{6}$$

above which thermal fluctuations are no longer significant. This transition scale can be used to define the thermal length scale

$$\ell_{\rm th} \equiv \frac{2\pi}{q_{\rm th}} = \sqrt{\frac{64\pi^3\kappa_0^2}{3k_BTY_0}} \tag{7}$$

beyond which thermal fluctuations become important.

The scaling functions for the renormalized elastic constants in Eq. (5) are presented in Fig. 1(d–f). Note that in the long wavelength limit ($q \ll q_{\rm th}$) these scaling functions are universal and they hold for all isotropic microscopic sheets, where the continuum theory applies, i.e. for wave vectors q that are much smaller than the microscopic cutoff $\Lambda \sim 1/a_0$, where a_0 is e.g. the lattice spacing in 2D crystalline sheets. Note that in the long wavelength limit the renormalized Poisson's ratio approaches the universal value of $-1/3$ regardless of the zero temperature value ν_0 of the Poisson's ratio. The universal negative Poisson's ratio was first predicted by the self consistent scaling analysis (Le Doussal and Radzihovsky, 1992), which was confirmed by Monte Carlo simulations (Falcioni et al., 1997). Note also that due to thermal fluctuations the microscopically anisotropic sheets, such as black phosphorene, behave like isotropic sheets in the long wavelength limit (Toner, 1989). At room temperatures thermal fluctuations are important for freely suspended 2D crystalline sheets, such as graphene ($\ell_{\rm th} \approx 4$ nm, Fasolino et al. (2007), Lee et al. (2008)) or MoS_2 ($\ell_{\rm th} \approx 40$–50 nm, Bertolazzi et al. (2011), Lai et al. (2016)), which can easily be fabricated on the microscale. Thus thermal fluctuations in these systems significantly increase the bending rigidity and reduce the Young's and shear moduli (see Fig. 1). Furthermore, the characteristic diameter of clay platelets is ≈ 100–500 nm, which is comparable to the thermal length scale $\ell_{\rm th} \approx 100$–$1000$ nm at room temperature (Suter et al., 2007; Ploehn and Liu, 2006). Similarly, the diameter of red blood cells

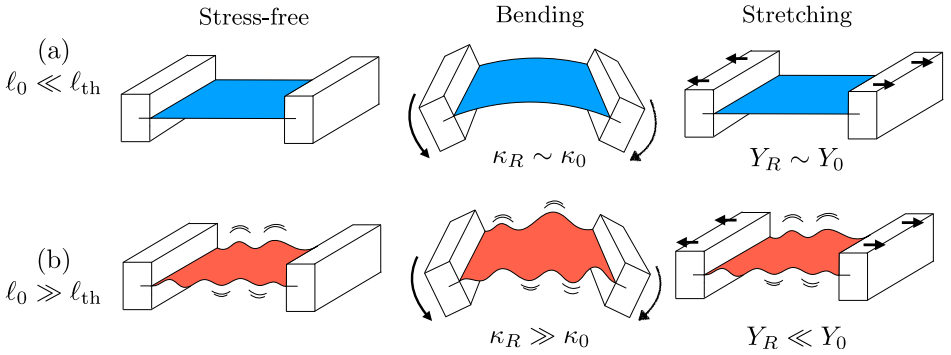

Fig. 2. Schematic of mechanical properties of fluctuating sheets that are (a) smaller and (b) larger than the thermal lengthscale $\ell_{\rm th}$, where the amplitude of height fluctuations is smaller and larger than the sheet thickness, respectively. Height fluctuations that are larger than the sheet thickness make the sheet effectively stiffer for bending and softer for stretching as discussed in the main text.

(6–8 μm) is comparable to the thermal length scale $\ell_{\rm th} \approx$ 2–10 μm at room temperature (Waugh and Evans, 1979; Evans, 1983; Park et al., 2010; Evans et al., 2017).

The stiffening of the renormalized bending rigidity and the softening of the in-plane elastic constants beyond the characteristic thermal lengthscale $\ell_{\rm th}$ can be intuitively understood in the following way (see Fig. 2). The amplitude of height fluctuations $\sqrt{\langle h(\mathbf{r})^2\rangle}$ increases with the scale ℓ as $\sqrt{\langle h(\mathbf{r})^2\rangle} \sim \ell\sqrt{k_BT/\kappa_0}$, where the effects of renormalization have been neglected. On scales shorter than the thermal lengthscale ($\ell \ll \ell_{\rm th}$), the amplitude of height fluctuations is much smaller than the sheet thickness ($\sim \sqrt{\kappa_0/Y_0}$) and such fluctuating sheets mechanically behave like classical plates. Conversely, on scales larger than the thermal lengthscale ($\ell \gg \ell_{\rm th}$), the amplitude of height fluctuations is much larger than the sheet thickness. Such fluctuating sheets are much harder to bend due to the induced Gaussian curvature, which requires stretching of the sheet. On the other hand, such fluctuating sheets are easier to stretch, because this requires flattening of the entropic "wrinkles" rather than stretching the material. The effective stiffening of the bending rigidity and the softening of the in-plane elastic constants, scales with some power of the amplitude of height fluctuations $\sqrt{\langle h(\mathbf{r})^2\rangle}$, which explains the observed power-law scalings in Fig. 1d–f. The origin of this effective behavior is the non-linear coupling between the in-plane displacements $u_i(\mathbf{r})$ and the out-of-plane displacements $h(\mathbf{r})$ in the strain tensor u_{ij} in Eq. (2).

3. Buckling of fluctuating sheets

When the external load σ_{ij} ($i, j \in \{x, y\}$) is applied to the boundary of the elastic sheet, the spectrum of height fluctuations becomes (Roldan et al., 2011; Košmrlj and Nelson, 2016)

$$G_{hh}(\mathbf{q}) = \langle h(\mathbf{q})h(-\mathbf{q})\rangle = \frac{k_BT}{A\left[\kappa_R(q)q^4 + \sigma_{ij}q_iq_j\right]}. \tag{8}$$

Note that for sufficiently large compressive loads (negative σ_{xx} and/or σ_{yy}) or shear loads ($\sigma_{xy} \neq 0$) the denominator in Eq. (8) can become negative, which reflects the fact that the flat state becomes unstable and the sheet buckles. The critical buckling load σ_R^b corresponds to the minimum compressive load, where the denominator in Eq. (8) vanishes. Note that the applied external load could affect the renormalization of the bending rigidity $\kappa_R(q)$ as was previously demonstrated for sheets under tension (Guitter et al., 1989; Morse and Lubensky, 1992; Radzihovsky and Toner, 1998; Košmrlj and Nelson, 2016; Burmistrov et al., 2018). This effect becomes important when the contribution from external load in the denominator of Eq. (8) becomes dominant, which happens only after the sheet buckles. Thus we expect that the renormalization of the bending rigidity is not significantly affected up to the critical buckling load, but it is likely affected in the post-buckling regime.

Here, we consider the buckling of a square sheet of size $\ell_0 \times \ell_0$ with periodic boundary conditions for the biaxial and uniaxial compression, and pure shear, as well as the clamped-free boundary conditions for the uniaxial compression (two edges that experience the load are clamped, while the other two edges are free). For the biaxial compression ($\sigma_{xx} = \sigma_{yy} = -\sigma$, $\sigma_{xy} = 0$) and the uniaxial compression ($\sigma_{xx} = -\sigma$, $\sigma_{yy} = \sigma_{xy} = 0$), the critical buckling load is $\sigma_R^b = \kappa_R(q_{\rm min})q_{\rm min}^2$, where $q_{\rm min} = 2\pi/\ell_0$ is the smallest wave vector allowed by the boundary conditions. For the pure shear ($\sigma_{xy} = \sigma$, $\sigma_{xx} = \sigma_{yy} = 0$) the critical buckling load is $\sigma_R^b = 2\kappa_R(q_{\rm min})q_{\rm min}^2$ and the buckled mode corresponds to $q_x = q_y = q_{\rm min}$. The critical buckling load σ_R^b thus scales as

$$\sigma_R^b = C\kappa_R(q_{\rm min})q_{\rm min}^2 \sim \begin{cases} \kappa_0\ell_0^{-2}, & \ell_0 \ll \ell_{\rm th} \\ \kappa_0\ell_0^{-2+\eta}\ell_{\rm th}^{-\eta}, & \ell_0 \gg \ell_{\rm th} \end{cases}, \tag{9}$$

where $C = 1$ for the biaxial and uniaxial compression and $C = 2$ for the pure shear. Note that the critical buckling load is temperature dependent and scales as $\sigma_R^b \sim T^{\eta/2}$ for elastic sheets that are larger than the thermal length scale ($\ell_0 \gg \ell_{\rm th}$), e.g. graphene,

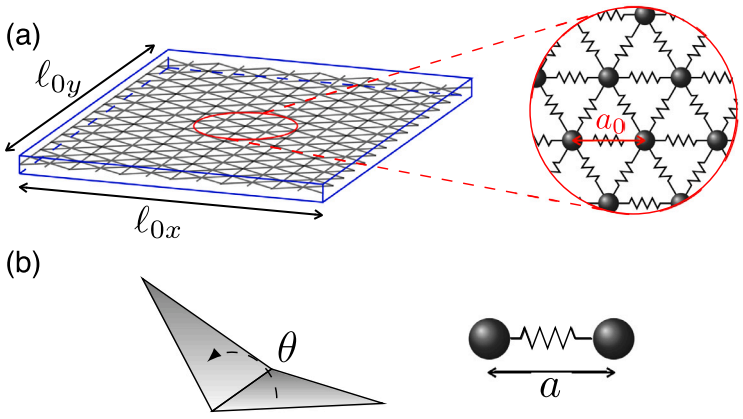

Fig. 3. (a) An elastic sheet is represented as an equilateral triangulation of a rectangle with size $\ell_{0x} \times \ell_{0y}$ ($\ell_{0x} \approx \ell_{0y}$) where particles are positioned on lattice points with bending and stretching energies defined along the edges and plaquettes of the triangulation. (b) The bending energy is described as a penalty of changing the dihedral angle θ between two triangles sharing an edge. The stretching energy is described as a penalty of changing the bond length a between the two particles from the rest length a_0.

MoS_2, and other 2D crystalline materials. Compared to the classical value for the critical buckling load $\sigma_0^b = 4\pi C\kappa_0/\ell_0^2$ at zero temperature (Timoshenko and Woinowsky-Krieger, 1959; van der Heijden, 2009), thermal fluctuations effectively increase the critical buckling load due to the enhanced renormalized bending rigidity as

$$\frac{\sigma_R^b}{\sigma_0^b} = \frac{\kappa_R(q_{\min})}{\kappa_0} \equiv \frac{\overline{\kappa}_R(\ell_0)}{\kappa_0}. \tag{10}$$

Note that thermal fluctuations reduce the projected length of the square sheet by $\langle \Delta\ell \rangle \sim -(k_B T/\kappa)\ell_0$ (Košmrlj and Nelson, 2016), which could also affect the critical buckling load. However, for typical 2D crystalline materials $k_B T/\kappa \ll 1$ at room temperature and this effect is negligible compared to the significantly enhanced renormalized bending rigidity for $\ell_0 \gg \ell_{\text{th}}$. Note also that the enhanced critical buckling load for flat sheets is qualitatively different from spherical shells, where thermal fluctuations effectively reduce the critical buckling pressure (Paulose et al., 2012; Košmrlj and Nelson, 2017; Baumgarten and Kierfeld, 2018; Singh et al., 2020). Spherical shells under pressure are metastable and thermal fluctuations can make them cross the energy barrier even below the classical buckling pressure, which corresponds to the limit of metastability (Baumgarten and Kierfeld, 2018). In contrast, the flat state of compressed sheets is globally stable up to the critical buckling load.

3.1. Molecular dynamics simulations

To test the prediction for the critical buckling load in Eq. (9) we performed coarse-grained Molecular Dynamics simulations, where the elastic sheet is discretized as a triangulation of a nearly square sheet of size $\ell_{0x} \times \ell_{0y}$ with $\ell_{0x} \approx \ell_{0y}$ (see Fig. 3). Such simulations were previously used to test the renormalization of elastic constants (Zhang et al., 1993; Bowick et al., 1996, 1997, 2017) and they agreed very well with both the continuum theory and the atomistic Monte Carlo simulations (Los et al., 2009; Roldan et al., 2011; Los et al., 2016) on scales that are much larger than the lattice constant and interatomic spacing.

In the undeformed flat configuration, all triangles are equilateral with the edge length a_0. The bending and stretching energies are described using a common discretization (Seung and Nelson, 1988) of the continuum energy in Eq. (1) as

$$\begin{aligned} E_{\text{bend}} &= \sum_{\langle I,J \rangle} k_{\text{bend}}(1 + \cos\theta_{IJ}), \\ E_{\text{stretch}} &= \sum_{\langle i,j \rangle} \frac{1}{2} k_{\text{stretch}}(a_{ij} - a_0)^2, \end{aligned} \tag{11}$$

where θ_{IJ} is the dihedral angle between the neighbor triangles I and J that are sharing an edge, and $a_{ij} = |\mathbf{r}_i - \mathbf{r}_j|$ is the Euclidean distance between the nearest-neighbor particles i and j. Note that the discretization parameters k_{bend} and k_{stretch} are directly related to the continuum bending rigidity $\kappa_0 = \frac{\sqrt{3}}{2} k_{\text{bend}}$, the continuum Young's modulus $Y_0 = \frac{2}{\sqrt{3}} k_{\text{stretch}}$, and the continuum Poisson's ratio $\nu_0 = 1/3$ (Seung and Nelson, 1988; Schmidt and Fraternali, 2012). In the Appendix A we show that this discretized model recapitulates the zero temperature stress–strain curves for the buckling of sheets under biaxial compression and pure shear obtained with standard finite element methods (see Fig. A.6).

Molecular Dynamics simulations at finite temperatures were performed using the LAMMPS package (Plimpton (1995), see Appendix B for details). Unless otherwise noted the undeformed size of the sheet was $\ell_0 = 100\, a_0$ ($\ell_{0x} = 116\, a_0\sqrt{3}/2 \approx 100.5\, a_0$ and $\ell_{0y} = 100\, a_0$). To adjust the thermal length scale $\ell_{\text{th}} \sim \kappa_0/\sqrt{k_B T Y_0}$ we varied the temperature T, and the bending and stretching spring constants k_{bend} and k_{stretch}, respectively, which enabled us to explore a wide range of thermal length scales

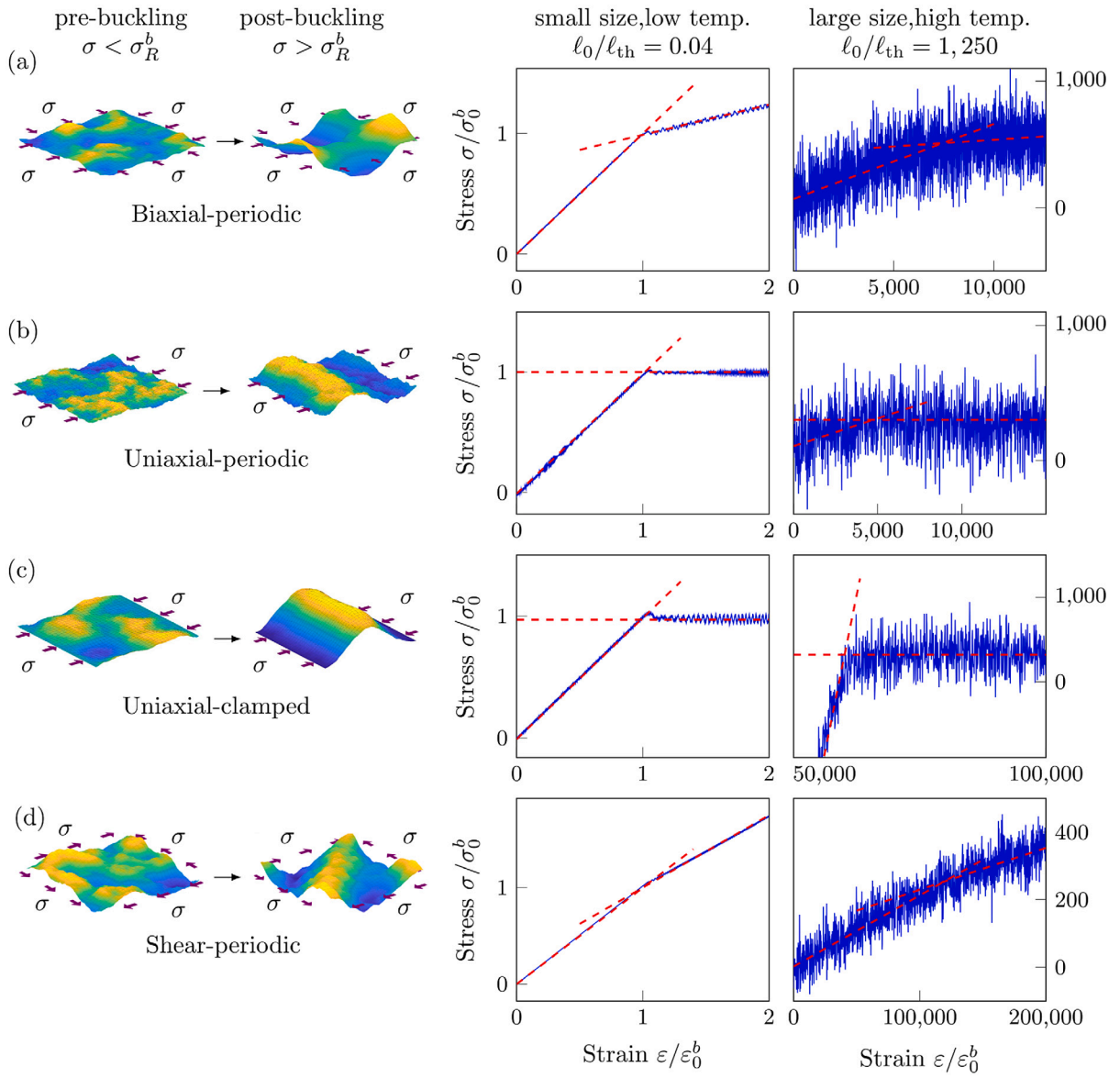

Fig. 4. Representative simulation results for (a) biaxially compressed sheet with periodic boundary conditions, (b) uniaxially compressed sheet with periodic boundary conditions, (c) uniaxially compressed sheet with clamped-free boundary conditions, and (d) sheet under pure shear with periodic boundary conditions. Snapshots on the left show typical sheet configurations pre- and post-buckling. For clarity, the height profiles of sheets (z coordinates) are also indicated by a heat map, where yellow indicates the largest heights and dark blue indicates the lowest heights. Plots in the middle and right columns show characteristic stress–strain curves at low temperature ($\ell_0/\ell_{\rm th} = 0.04$) and at high temperature ($\ell_0/\ell_{\rm th} = 1250$), respectively, where stresses are averaged over 30 simulation runs. Red dashed lines show linear fits to the first 600 (pre-buckling) and to the last 900 points (post-buckling) out of total 3000 points. For compressed sheets with periodic boundary conditions we plot relative strains $\epsilon = (\langle \ell_x(\sigma = 0)\rangle - \ell_x)/\ell_{0x}$, where ℓ_{0x} and ℓ_x are the undeformed and the deformed lengths of the sheet, respectively, and $\langle \ell_x(\sigma = 0)\rangle$ corresponds to the equilibrium length of the sheet at zero load. For clamped boundary conditions we plot absolute strains $\epsilon = (\ell_{0x} - \ell_x)/\ell_{0x}$. For sheets under pure shear we plot shear strain $\epsilon = \gamma/2$, where γ is the shear angle. Stresses σ are normalized with the zero temperature critical buckling load $\sigma_0^b = 4\pi C\kappa_0/\ell_0^2$. Strains ϵ are normalized with the zero temperature critical buckling strains ϵ_0^b, which are $\epsilon_0^b = \sigma_0^b/Y_0$ for the uniaxial compression, $\epsilon_0^b = \sigma_0^b/(2B_0)$ for the biaxial compression, and $\epsilon_0^b = \sigma_0^b/(2\mu_0)$ for pure shear, where $B_0 = Y_0/[2(1 - \nu_0)]$ is the 2D bulk modulus and $\nu_0 = 1/3$ is the Poisson's ratio.

($\ell_0/\ell_{\rm th} \in (10^{-2}, 10^5)$, see Table B.1 in Appendix). Simulations in the absence of external loads were used to verify the scaling of correlation functions and renormalized elastic constants in Eqs. (4) and (5) (see Fig. 1).

Fig. 4 shows typical stress–strain curves at low temperature ($\ell_0/\ell_{\rm th} = 0.04$) and at high temperature ($\ell_0/\ell_{\rm th} = 1250$) for 4 different loading and boundary conditions, where compressive and shear strains were prescribed and were gradually increased in 3000 increments, while allowing the sheet to equilibrate for 5000 time steps between each increment. Stresses were calculated using

the virial stress equation as described in the Appendix B and averaged over 30 independent simulation runs. We checked that the results were insensitive to the effective strain rate (see Fig. B.7 in Appendix). Note that for the biaxially and uniaxially compressed sheets with periodic boundary conditions we plotted relative strains that are calculated relative to the projected equilibrium sheet length $\langle \ell_x(\sigma = 0)\rangle$ at zero load, which was obtained with an initial NPT simulation. The projected equilibrium sheet length $\langle \ell_x(\sigma = 0)\rangle$ is smaller than the undeformed sheet length ℓ_{0x} due to the out-of-plane fluctuations (De Andres et al., 2012; Košmrlj and Nelson, 2016; Amorim et al., 2016; Liang and Purohit, 2016). For the clamped boundary condition we were unable to perform NPT-like simulations. Thus we plotted absolute strains that are calculated relative to the undeformed sheet length ℓ_{0x}. Note that the sheet is under tension at zero absolute strain (negative stress values in Fig. 4c) because thermal fluctuations cause shrinking of the sheet, which has to be then pulled back to the initial length.

At low temperatures ($\ell_0/\ell_{\text{th}} = 0.04$ in Fig. 4) we recover classical results (Timoshenko and Woinowsky-Krieger, 1959; van der Heijden, 2009). In the pre-buckling regime, the slopes for the uniaxially and biaxially compressed sheets are equal to Y_0 and $2B_0$, respectively, where $B_0 = Y_0/[2(1-\nu_0)]$ is the 2D bulk modulus and $\nu_0 = 1/3$ is the Poisson's ratio. In the post-buckling regime, the slope is zero for the uniaxially compressed sheets, but non-zero for the biaxially compressed sheets. This is because at the critical buckling load $\sigma_0^b = 4\pi\kappa_0/\ell_0^2$ only one mode ($\mathbf{q}_1 = (2\pi/\ell_{0x}, 0)$) becomes unstable for the uniaxial compression (see Fig. 4b,c), while two modes ($\mathbf{q}_1 = (2\pi/\ell_{0x}, 0)$ and $\mathbf{q}_2 = (0, 2\pi/\ell_{0y})$) become unstable for the biaxial compression (see Fig. 4a). The linear combination of the two unstable modes produces Gaussian curvature, which forces the sheet to stretch and the resulting slope is reduced to $B_0/2$ (Timoshenko and Woinowsky-Krieger, 1959; van der Heijden, 2009). For sheets under pure shear, the slope in the pre-buckling regime is $2\mu_0$ and reduces to $(4/3)\mu_0$ in the post-buckling regime (see Fig. 4d), where $\mu_0 = Y_0/[2(1+\nu_0)]$ is the 2D shear modulus. Note that at low temperatures we observe periodic oscillations in the stress–strain curves (see $\ell_0/\ell_{\text{th}} = 0.04$ in Fig. 4). This is because the auto-correlation times for the soft long wavelength modes are very long and we were unable to fully equilibrate the sheet (see Fig. B.8 in Appendix).

At high temperatures ($\ell_0/\ell_{\text{th}} = 1250$ in Fig. 4) the stress–strain curves exhibit larger fluctuations because the amplitude of thermal fluctuations is increased, but we can still identify two different regimes (fitted red dashed lines in Fig. 4) at low strains and large strains, which correspond to the pre-buckling and post-buckling regimes. The slopes in the pre-buckling regime for the uniaxially and biaxially compressed sheets correspond to the renormalized Young's modulus and bulk modulus, respectively, while for sheets under pure shear they correspond to the renormalized shear modulus (see Fig. B.9 in Appendix). Note that the renormalized Young's modulus, bulk, and shear moduli are reduced compared to the zero temperature values (see Fig. 1), which is reflected in the fact that slopes are less than 1 in the normalized stress–strain curves in Fig. 4. Furthermore, the critical buckling load (intersection of two fitted red dashed lines) is significantly increased compared to the zero temperature value as we predicted in Eq. (10).

Finally, in Fig. 5 we compare the critical buckling load σ_R^b obtained from the stress–strain curves (see Fig. 4) with the theoretical predictions in Eq. (10). For the biaxially compressed sheets and sheets under shear the critical buckling loads and the confidence intervals were obtained by the intersections of two lines that correspond to the fits for the pre- and post-buckling regime (see Fig. 4a,d). For the uniaxially compressed samples, the value of stress levels off in the post-buckling regime (see Fig. 4b,c). Thus we estimated the critical buckling load and confidence intervals by doing long simulations at the maximum compressive strain in the post-buckling regime (see Appendix B for details).

By varying the size of the sheet ℓ_0, the ambient temperature T, and the spring constants k_{bend} and k_{stretch} for the bending and stretching, respectively, we are able to tune the ratio of ℓ_0/ℓ_{th} by 7 orders of magnitude ($\ell_0/\ell_{\text{th}} \in (10^{-2}, 10^5)$). All the values for critical buckling loads can be collapsed to a single scaling function (see Fig. 5) as predicted by the theory in Eq. (10).

For sheets with periodic boundary conditions we get a remarkably good agreement with the theoretical predictions, which confirms that thermal fluctuations increase the critical buckling load due to the enhanced renormalized bending rigidity (see Fig. 5). Recall that we were unable to fully equilibrate simulations at low temperatures (oscillations for $\ell_0/\ell_{\text{th}} = 0.04$ in Fig. 4), but in this regime the effects of thermal fluctuations are small and the critical buckling loads σ_R^b are well approximated by the classical critical buckling load $\sigma_0^b = 4\pi C\kappa_0/\ell_0^2$. At very large temperatures ($\ell_0/\ell_{\text{th}} \gtrsim 10^4$) we observe systematic deviation from the theoretical prediction. Inspection of the sheet configurations revealed that the local bond strains fluctuate by ±5–10% and that the local dihedral angles fluctuate by ±20°. For such large fluctuations the discretized energy in Eq. (11) starts deviating from the linear elastic sheet that was assumed for theoretical calculation. Furthermore, according to the Lindemann criterion (Lindemann, 1910; Born, 1939), such large fluctuations would cause the sheet to melt, which was prevented in our simulations, where the connectivity between particles was fixed. Melting of fluctuating sheets is still an unresolved problem and we leave this for future work.

For the uniaxially compressed sheets with clamped boundary condition, we also observe a scaling collapse of the critical buckling load (Fig. 5c). However, we notice a systematic deviation from the theoretical prediction in Eq. (10). In previous studies of thermalized ribbons it was noted that the effect of clamped boundaries decays in the bulk with the scale that is of the order of the width of the ribbon (Bowick et al., 2017; Wan et al., 2017; Russell et al., 2017). Thus the effect of clamped boundaries is felt throughout the square sheets, which affects the renormalization of the bending rigidity in the bulk. Nonetheless, in this case we still see that thermal fluctuations can significantly increase the critical buckling load for large values of ℓ_0/ℓ_{th}.

4. Conclusions

The results presented above are universal and they hold for any free-standing elastic sheet, where the continuum theory applies, i.e. when the sheet is much larger than the microscopic cutoff, e.g. the interatomic spacing in 2D crystalline sheets. For sheets that are much smaller than the thermal length scale $\ell_{\text{th}} \sim \kappa_0/\sqrt{k_B T Y_0}$ thermal fluctuations are negligible and classical mechanics applies. This is the case for all macroscopic sheets and plates because the thermal length scale rapidly increases with the sheet thickness t and

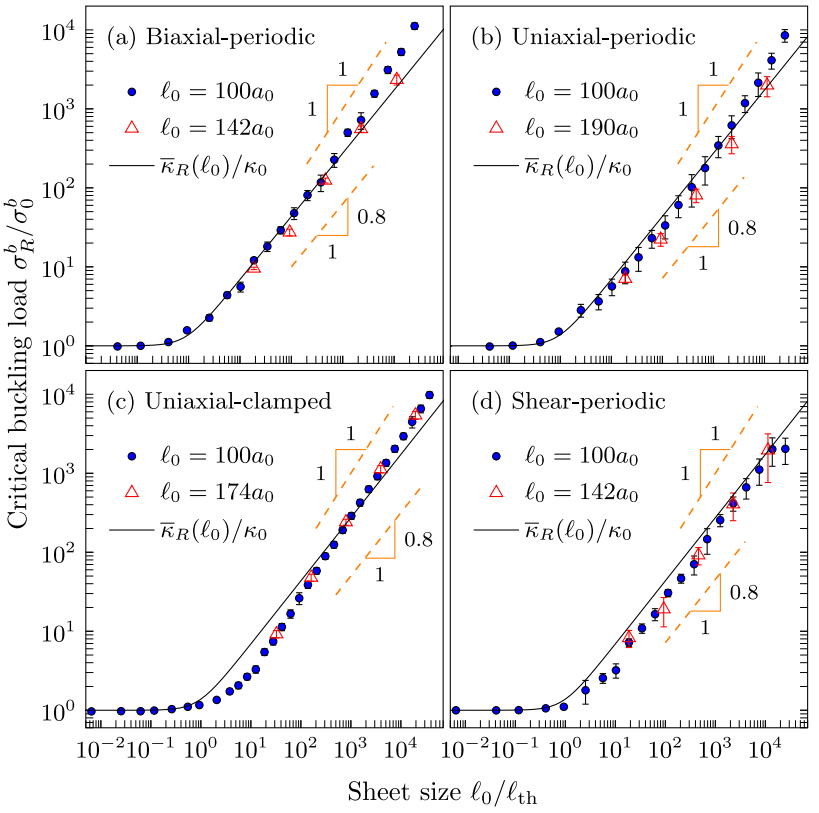

Fig. 5. Scaling functions for the critical buckling load σ_R^b for (a) biaxially compressed sheets with periodic boundary conditions, (b) uniaxially compressed sheets with periodic boundary conditions, (c) uniaxially compressed sheets with clamped-free boundary conditions, and (d) periodic sheet under pure shear. The critical buckling loads σ_R^b and confidence intervals (errorbars) were obtained from the stress–strain curves in Fig. 4. Simulations were done for two different sheet sizes ℓ_0 (blue dots and red triangles) and thermal length scale $\ell_{\rm th}$ defined in Eq. (7) was tuned by varying the temperature T, and the spring constants $k_{\rm bend}$ and $k_{\rm stretch}$ for the bending and stretching. The critical buckling loads σ_R^b were normalized by the classical zero temperature value $\sigma_0^b = 4\pi C\kappa_0/\ell_0^2$ and plotted as a function of the normalized sheet size $\ell_0/\ell_{\rm th}$. Solid black line shows the theoretical prediction from Eq. (10), where we used the renormalized bending rigidity from Fig. 1d. The orange lines serve as a guide to the eye for different power-law exponents.

scales as $\ell_{\rm th} \sim t^{5/2}E^{1/2}(k_BT)^{-1/2}$, where E is the 3D Young's modulus ($\kappa_0 \sim Et^3$, $Y_0 \sim Et$). As the sheet thickness is reduced to the order of nanometers, as is the case for clay plates and red blood cells, the thermal length scale $\ell_{\rm th}$ becomes comparable to the size ℓ_0 of the sheet. In this regime thermal fluctuations become relevant and the renormalized bending rigidity and the critical buckling load are mildly increased (Fig. 5). Note that in red blood cells the molecular activity produces non-equilibrium fluctuations, which dominate over the thermal fluctuations on large length scales as was deduced from the breakdown of the fluctuation–dissipation theorem (Turlier et al., 2016). In the future it would thus be worth exploring how such dynamic non-equilibrium fluctuations affect the mechanical properties of slender structures.

As the sheet thickness is reduced to the atomistic scale, such as for graphene, boron nitride, transition metal dichalcogenide, and other 2D materials, the thermal length scale becomes of the order of nanometers at room temperature, which is much smaller than the characteristic size of these sheets. In this regime thermal fluctuations significantly increase the critical buckling load ($\ell_0/\ell_{\rm th} \gg 1$ in Fig. 5), which becomes temperature dependent and scales as $\sigma_R^b \sim \overline{\kappa}_R(\ell_0)\ell_0^{-2} \sim \kappa_0\ell_0^{-2+\eta}\ell_{\rm th}^{-\eta} \sim \kappa_0^{1-\eta}\ell_0^{-2+\eta}(k_BTY_0)^{\eta/2}$. In this work we focused on the buckling of thermalized square sheets and in the future it would be interesting to explore the effect of sheet geometry. For narrow ribbons with the width W and length $\ell_0 \gtrsim W$ it was previously shown that thermal fluctuations renormalize the bending rigidity up to the scale of the ribbon width (Košmrlj and Nelson, 2016). The critical buckling load for ribbons compressed uniaxially along the long axis is thus expected to scale as $\sigma_R^b \sim \overline{\kappa}_R(W)\ell_0^{-2}$, which was recently explored by Hanakata et al. (2020). In this work we focused on pristine elastic sheets, but defects are often unavoidable in 2D materials and they produce static ripples. It was previously demonstrated that quenched defects also enhance the bending rigidity and they can dominate over the thermal fluctuations when the amplitudes of static ripples is larger than the amplitude of height fluctuations due to temperature (Nelson and Radzihovsky, 1991; Radzihovsky and Nelson, 1991; Morse and Lubensky, 1992; Le Doussal and Radzihovsky, 1993; Košmrlj and Nelson, 2013, 2014; Gornyi et al., 2015; Le Doussal and Radzihovsky, 2018). Since the critical buckling load studied in this work scales with the effective bending rigidity, we expect that defects and static ripples will also increase the critical buckling load. Moreover, the static ripples and other mechanical deformations in 2D materials can affect their electronic transport (Mariani and von Oppen, 2008; Castro et al., 2010; Mariani and von Oppen, 2010; Guinea et al., 2008, 2009; Castro Neto et al., 2009; Amorim et al.,

2016). The coupling between elastic deformations and the electronic degrees of freedom could also affect the effective mechanical behavior of suspended membranes (Gazit, 2009a,b; San-Jose et al., 2011; Guinea et al., 2014; González, 2014). In particular, they could produce spontaneous buckling (Bonilla and Ruiz-Garcia, 2016; Ruiz-García et al., 2016; Ruiz-Garcia et al., 2017) and stable ripples (Cea et al., 2020; Ruiz-García et al., 2015).

We hope this work will stimulate further experimental, numerical, and theoretical investigations of the stability and mechanical properties of thermalized sheets as well as extensions to more complicated geometries found in microscopic kirigami and origami structures.

CRediT authorship contribution statement

Ali Morshedifard: Methodology, Software, Investigation, Data curation, writing - original draft, Writing - review & editing, Visualization. **Miguel Ruiz-García:** Methodology, Formal analysis, Investigation, Writing - original draft, Writing - review & editing. **Mohammad Javad Abdolhosseini Qomi:** Conceptualization, Methodology, Writing - review & editing, Supervision, Project administration, Funding acquisition. **Andrej Košmrlj:** Conceptualization, Methodology, Formal analysis, Writing - review & editing, Supervision, Project administration, Funding acquisition.

Declaration of competing interest

The authors declare that they have no known competing financial interests or personal relationships that could have appeared to influence the work reported in this paper.

Acknowledgments

This work was supported by National Science Foundation, USA through the Career Award DMR-1752100 (A.K.), the Grant No. CMMI-1826122 (M.J.A.Q.), and the Grant No. DMR-1506625 (M.R.-G.). M.R.-G. also acknowledges support from the Simons Foundation, USA via awards 327939 and 454945.

Appendix A. Comparison of athermal behavior of the coarse-grained model with nonlinear finite elements

To show the equivalence of the coarse-grained model used in this study with the classical plate theory, we compared the pre- and post-buckling behavior of a periodic sheet under biaxial compression or pure shear at zero temperature with a geometrically nonlinear finite element (FE) solution via Abaqus. We used the Mindlin–Reissner quadratic shell elements (S8R) combined with a nonlinear solver that allowed for large displacements, strains and large rotations. Constraints were applied to degrees of freedom on the edges to simulate periodic boundary conditions. The plate was incrementally strained biaxially in a nonlinear FE solver to about twice the critical buckling strain to observe the post-buckling behavior. Similarly, we incrementally increased shear strain in a nonlinear FE solver to observe the post-buckling behavior. The resulting stress–strain curves in Fig. A.6 obtained with geometrically nonlinear FE showed an excellent agreement with our discretized model in both the pre- and post-buckling regimes.

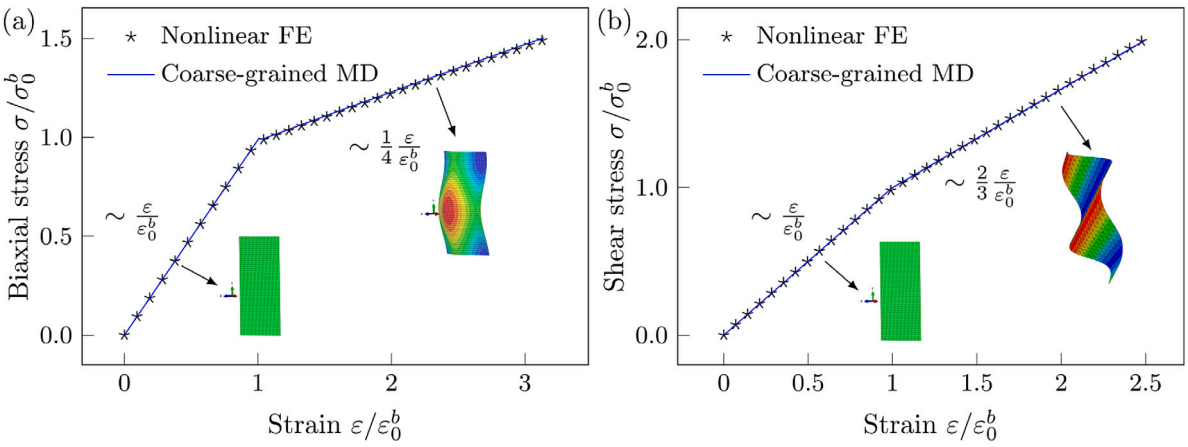

Fig. A.6. Stress–strain curves for sheets under (a) biaxial compression and (b) pure shear, both with periodic boundary conditions, obtained with nonlinear finite element (FE) calculations and coarse-grained molecular dynamics (MD) simulations. Stresses σ are normalized with the zero temperature critical buckling load $\sigma_0^b = 4\pi C\kappa_0/\ell_0^2$. Strains ϵ are normalized with the zero temperature critical buckling strains ϵ_0^b, which are $\epsilon_0^b = \sigma_0^b/(2B_0)$ for the biaxial compression, and $\epsilon_0^b = \sigma_0^b/(2\mu_0)$ for pure shear.

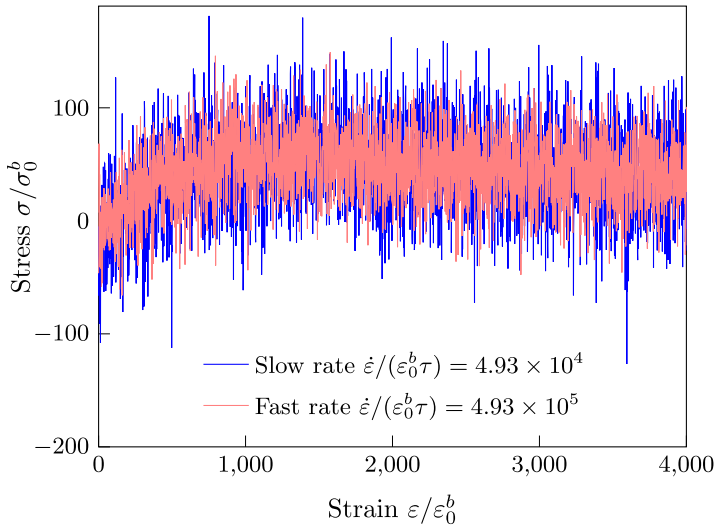

Fig. B.7. Stress–strain curves for a periodic sheet with $\ell_0/\ell_{\text{th}} = 206.3$ under uniaxial compression, where the slow and fast rates correspond to 50,000 and 5000 equilibration steps between successive compression increments. Strain rate $\dot{\epsilon}$ is normalized by the characteristic unit of time τ and the zero temperature critical buckling strain ϵ_0^b.

Table B.1
Parameters used in simulations ($a_0 = 2.46$ Å, $m = 24.02$ g/mol).

Index	T [K]	k_{stretch} [kcal/mol Å^2]	k_{bend} [kcal/mol]	ℓ_0/ℓ_{th}
1	0.3	20	200	0.00648
2	1	180	171.7	0.04135
3	5	200	143.4	0.1167
4	5	200	41.28	0.4052
5	10	31.02	10	0.9319
6	20	114.6	10	2.533
7	100	113.5	10	5.637
8	100	377	10	10.27
9	200	625.8	10	18.72
10	200	519.4	5	34.10
11	300	1150	5	62.14
12	300	610.7	2	113.2
13	500	1217	2	206.3
14	500	1010	1	375.9
15	600	698.5	0.5	685.0
16	600	2319	0.5	1248
17	1200	962.5	0.25	2274
18	2000	1917	0.25	4144
19	2000	1019	0.1	7551
20	2000	845.4	0.05	13 760
21	2000	2807	0.05	25 070

Appendix B. Coarse-grained molecular dynamics simulations

Coarse-grained molecular dynamics (MD) simulations were performed using the LAMMPS package (Plimpton, 1995). We chose the lattice constant a_0, the particle mass m, and k_BT as the fundamental units for length, mass, and energy, respectively. The units of time and stress were $\tau = a_0\sqrt{m/k_BT}$ and $\sigma = k_BT/a_0^2$, respectively. The velocity Verlet algorithm was used for the integration of equations of motion with a timestep of $\Delta t = 0.005\tau$ and Nosé–Hoover thermostat and barostat (Tuckerman, 2010) were used to control the ambient temperature and pressure, where needed. For all simulations, we fix the box height in the z-direction, where periodic boundary conditions were used. In all simulations, stress components were computed using the virial stress equation (Tuckerman, 2010)

$$\sigma_{ij} = \frac{\ell_z}{V}\left[\sum_{k=1}^{N} m_k v_i^k v_j^k + \sum_{k=1}^{N} r_i^k f_j^k\right], \tag{B.1}$$

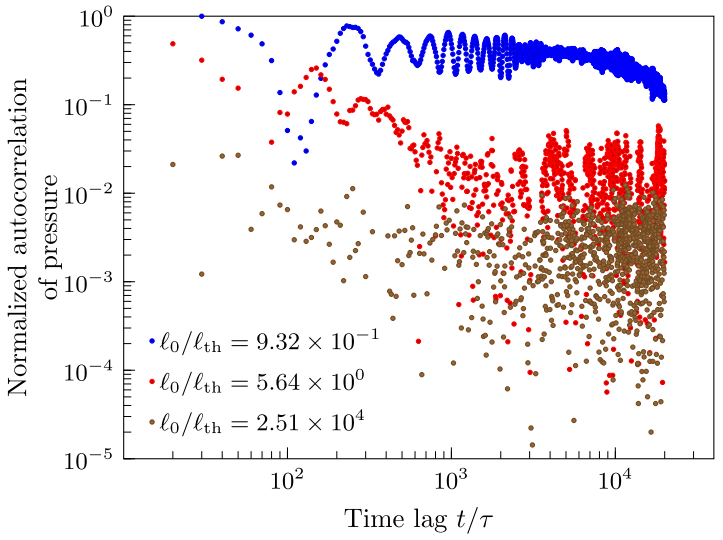

Fig. B.8. Autocorrelation of pressure for periodic sheets with high and low value of $\ell_0/\ell_{\rm th}$ under biaxial compression.

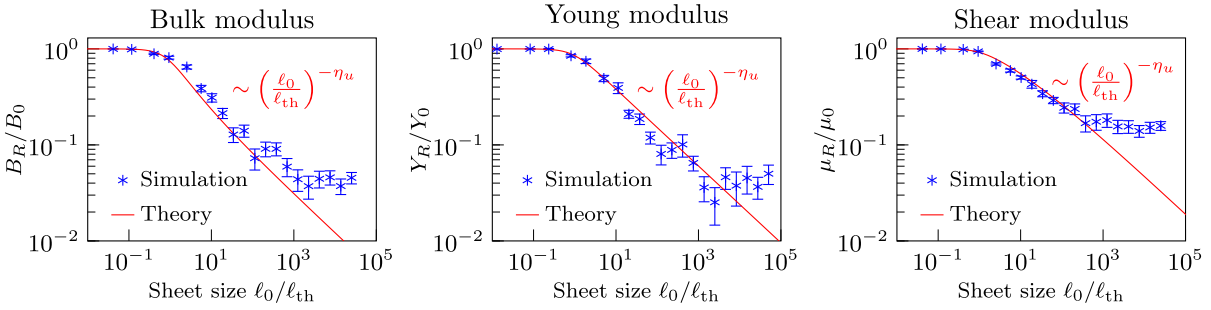

Fig. B.9. Rernormalized bulk (B_R), Young's (Y_R), and shear (μ_R) moduli obtained from the fitted slopes of the stress–strain curves in MD simulations and from the perturbative renormalization group procedure (Košmrlj and Nelson, 2016). For large sheets the renormalized elastic constants scale as $\sim (\ell_0/\ell_{\rm th})^{-\eta_u}$, where the exponent is $\eta_u \approx 0.3$–0.4. The systematic deviation in simulations for $\ell_0/\ell_{\rm th} \gtrsim 10^3$ is attributed to very high local strains as discussed in the main text.

where V and ℓ_z are the volume and the height of the simulation box, respectively, N is the number of particles, and v_i^k, r_i^k, and f_i^k are the ith component of the velocity, position, and resultant force for particle k, respectively. Parameters used in simulations are provided in Table B.1.

In simulations with periodic boundary conditions, we initially equilibrated the sheet by performing 2×10^6 time steps of NPT simulations at zero pressure such that $\langle \sigma_{xx} \rangle = \langle \sigma_{yy} \rangle = 0$. Subsequently, we gradually applied small strain increments to the system in 3000 steps, while allowing the sheet to equilibrate for 5000 time steps between each strain increment. Fig. B.7 shows that the stress–strain response of the sheet remains unaffected by reducing the strain rate by an order of magnitude.

For the biaxial compression scenario, we strain the system by prescribing the reduced box size in both x- and y-directions. For the uniaxial compression case, we strained the system by prescribing the reduced box size in the x-direction, while the box size in the y-direction was allowed to fluctuate such that $\langle \sigma_{yy} \rangle = 0$. For shear, the cubic box was tilted into a parallelepiped to prescribe the desired shear strain.

For simulations with clamped boundary conditions, we fixed two rows of particles along each of the two opposite edges. These particles were clamped in the x- and z-directions, but they were free to move in the y-direction. The other two edges were free to move and they were independent, i.e. they were not connected with periodic boundary condition. For these simulations, we gradually strained the system by bringing the two clamped edges closer together in 3000 increments, while allowing the sheet to equilibrate for 5000 time steps between each strain increment.

To ensure uncorrelated sampling from MD trajectories, the autocorrelation of the time series for any observable of interest (stress, strain, displacement, etc.) is computed as $r_m = c_m/c_0$, where $c_m = \frac{1}{(N-m)} \times \sum_{t=1}^{N-m} (y_t - \bar{y})(y_{t+m} - \bar{y})$, y is the observable, $\bar{y}$ is its average over a total of N time steps. Fig. B.8 shows the computed autocorrelation of pressure as a function of the autocorrelation lag time for biaxially compressed sheets with low, intermediate, and high values of $\ell_0/\ell_{\rm th}$. For high $\ell_0/\ell_{\rm th}$, there is a rapid relaxation of pressure, so that a large set of independent data can be obtained. However, for low $\ell_0/\ell_{\rm th}$, the relaxation time is several orders

of magnitude larger, which makes obtaining a proper uncorrelated sampling computationally unfeasible. However, since thermal fluctuations are negligible in this regime, it does not affect the simulations result in our study.

The critical buckling load for the uniaxially compressed sheets with periodic and clamped boundary conditions were calculated by performing 2×10^7 time steps at the maximum compressive strain and the average compressive stress was estimated using the virial stress equation. The errors of the critical loads were calculated as the standard errors of the mean for uncorrelated stress values taken every 10^6 time steps.

For sheets under biaxial compression and shear the critical buckling loads and the confidence intervals were obtained by the intersections of two lines that correspond to the fits for the pre- and post-buckling regime (see Fig. 4a,d), which were computed using the Statistics and Machine Learning Toolbox in MATLAB.

Finally, we also estimated the renormalized bulk, Young's, and shear moduli (see Fig. B.9) from the slopes of linear fits of the stress–strain curves in the pre-buckled regime for the periodic sheets under biaxial compression, uniaxial compression, and shear, respectively. At high temperature (high value of ℓ_0/ℓ_{th}) the stress–strain curves (see Fig. 4) are highly nonlinear and the fitted slopes are very sensitive to the number of data points. Thus, we fitted the slopes to either the initial 350 or 600 data points, which provided the upper and lower bounds for the estimated renormalized elastic constants.

References

Ahmadpoor, Fatemeh, Wang, Peng, Huang, Rui, Sharma, Pradeep, 2017. Thermal fluctuations and effective bending stiffness of elastic thin sheets and graphene: A nonlinear analysis. J. Mech. Phys. Solids 107, 294–319.

Amorim, B., Cortijo, A., Juan, F., de Grushin, A.G., Guinea, F., Gutierrez-Rubio, A., Ochoa, H., Parente, V., Roldan, R., San-Jose, P., Schiefele, J., Sturla, M., Vozmediano, M.A.H., 2016. Novel effects of strains in graphene and other two dimensional materials. Phys. Rep. 617, 1–54.

Aronovitz, J.A., Golubovic, L., Lubensky, T.C., 1989. Fluctuations and lower critical dimensions of crystalline membranes. J. Phys. (France) 50, 609–631.

Aronovitz, J.A., Lubensky, T.C., 1988. Fluctuations of solid membranes. Phys. Rev. Lett. 60, 2634–2637.

Baumgarten, Lorenz, Kierfeld, Jan, 2018. Buckling of thermally fluctuating spherical shells: Parameter renormalization and thermally activated barrier crossing. Phys. Rev. E 97 (5), 052801.

Bertolazzi, Simone, Brivio, Jacopo, Kis, Andras, 2011. Stretching and breaking of ultrathin MoS2. ACS Nano 5 (12), 9703–9709.

Bertoldi, Katia, Vitelli, Vincenzo, Christensen, Johan, Van Hecke, Martin, 2017. Flexible mechanical metamaterials. Nat. Rev. Mater. 2 (11), 1–11.

Blees, M.K., Barnard, A.W., Rose, P.A., Roberts, S.P., McGill, K.L., Huang, P.Y., Ruyack, A.R., Kevek, J.W., Kobrin, B., Muller, D.A., McEuen, P.L., 2015. Graphene kirigami. Nature 524, 204–207.

Bonilla, L.L., Ruiz-Garcia, M., 2016. Critical radius and temperature for buckling in graphene. Phys. Rev. B 93 (11), 115407.

Born, Max, 1939. Thermodynamics of crystals and melting. J. Chem. Phys. 7 (8), 591–603.

Bowick, M.J., Catterall, S.M., Falcioni, M., Thorleifsson, G., Anagnostopoulos, K.N., 1996. The flat phase of crystalline membranes. J. Phys. I 6, 1321–1345.

Bowick, M.J., Catterall, S.M., Falcioni, M., Thorleifsson, G., Anagnostopoulos, K., 1997. The flat phase of fixed-connectivity membranes. Nuclear Phys. B Proc. Suppl. 53, 746–752.

Bowick, M.J., Košmrlj, A., Nelson, D.R., Sknepnek, R., 2017. Non-hookean statistical mechanics of clamped graphene ribbons. Phys. Rev. B 95, 104109.

Brau, F., Damman, P., Diamant, H., Witten, T.A., 2013. Wrinkle to fold transition: influence of the substrate response. Soft Matter 9, 8177–8186.

Burmistrov, I.S., Gornyi, I.V., Kachorovskii, Yu, V., Katsnelson, M.I., Los, J.H., Mirlin, A.D., 2018. Stress-controlled Poisson ratio of a crystalline membrane: Application to graphene. Phys. Rev. B 97 (12), 125402.

Castro, Eduardo, V., Ochoa, H., Katsnelson, M.I., Gorbachev, R.V., Elias, D.C., Novoselov, K.S., Geim, A.K., Guinea, F., 2010. Limits on charge carrier mobility in suspended graphene due to flexural phonons. Phys. Rev. Lett. 105, 266601.

Castro Neto, A.H., Guinea, F., Peres, N.M.R., Novoselov, K.S., Geim, A.K., 2009. The electronic properties of graphene. Rev. Modern Phys. 81, 109–162.

Cea, T., Ruiz-García, M., Bonilla, L.L., Guinea, F., 2020. Numerical study of the rippling instability driven by electron–phonon coupling in graphene. Phys. Rev. B 101 (23), 235428.

Chopin, J., Kudrolli, A., 2013. Helicoids. Wrinkles, and Loops in Twisted Ribbons. Phys. Rev. Lett. 111, 174302.

Ciarlet, P.G., 2000. Mathematical Elasticity, Volume III: Theory of Shells. North Holland, Amsterdam.

Coquand, O., Mouhanna, D., Teber, S., 2020. Flat phase of polymerized membranes at two-loop order. Phys. Rev. E 101 (6), 062104.

De Andres, P.L., Guinea, F., Katsnelson, M.I., 2012. Bending modes, anharmonic effects, and thermal expansion coefficient in single-layer and multilayer graphene. Phys. Rev. B 86 (14), 144103.

Evans, E.A., 1983. Bending elastic modulus of red blood cell membrane derived from buckling instability in micropipet aspiration tests. Biophys. J. 43, 27–30.

Evans, A.A., Bhaduri, B., Popescu, G., Levine, A.J., 2017. Geometric localization of thermal fluctuations in red blood cells. Proc. Natl. Acad. Sci. USA 114, 2865–2870.

Falcioni, M., Bowick, M.J., Guitter, E., Thorleifsson, G., 1997. The Poisson ratio of crystalline surfaces. Europhys. Lett. 38, 67–72.

Fasolino, A., Los, J.H., Katsnelson, M.I., 2007. Intrinsic ripples in graphene. Nature Mater. 6 (858).

Gazit, Doron, 2009a. Correlation between charge inhomogeneities and structure in graphene and other electronic crystalline membranes. Phys. Rev. B 80, 161406.

Gazit, Doron, 2009b. Structure of physical crystalline membranes within the self-consistent screening approximation. Phys. Rev. E 80, 041117.

González, J., 2014. Rippling transition from electron-induced condensation of curvature field in graphene. Phys. Rev. B 90, 165402.

Gornyi, I.V., Kachorovskii, V.Y., Mirlin, A.D., 2015. Rippling and crumpling in disordered free-standing graphene. Phys. Rev. B 92, 155428.

Guinea, F., Horovitz, Baruch, Doussal, P. Le, 2009. Gauge fields, ripples and wrinkles in graphene layers. Solid State Commun. 149 (27), 1140–1143, Recent Progress in Graphene Studies.

Guinea, F., Horovitz, Baruch, Le Doussal, P., 2008. Gauge field induced by ripples in graphene. Phys. Rev. B 77, 205421.

Guinea, Francisco, Le Doussal, Pierre, Wiese, Kay Jörg, 2014. Collective excitations in a large-d model for graphene. Phys. Rev. B 89, 125428.

Guitter, E., David, F., Leibler, S., Peliti, L., 1988. Crumpling and buckling transitions in polymerized membranes. Phys. Rev. Lett. 61 (2949).

Guitter, E., David, F., Leibler, S., Peliti, L., 1989. Thermodynamical behavior of polymerized membranes. J. Phys. (France) 50, 1787–1819.

Hanakata, Paul Z., Bhabesh, Sourav S., Bowick, Mark J., Nelson, David R., Yllanes, David, 2020. Thermal buckling and symmetry-breaking in thin ribbons under compression. arXiv preprint arXiv:2012.06565.

Kadic, Muamer, Milton, Graeme W., van Hecke, Martin, Wegener, Martin, 2019. 3D metamaterials. Nat. Rev. Phys. 1 (3), 198–210.

Katsnelson, M.I., 2012. Graphene : Carbon in Two Dimensions. Cambridge University Press, New York.

Košmrlj, A., Nelson, D.R., 2013. Mechanical properties of warped membranes. Phys. Rev. E 88, 012136.

Košmrlj, A., Nelson, D.R., 2014. Thermal excitations of warped membranes. Phys. Rev. E 89, 022126.

Košmrlj, A., Nelson, D.R., 2016. Response of thermalized ribbons to pulling and bending. Phys. Rev. B 93, 125431.

Košmrlj, A., Nelson, D.R., 2017. Statistical mechanics of thin spherical shells. Phys. Rev. X 7, 011002.
Kownacki, J.-P., Mouhanna, D., 2009. Crumpling transition and flat phase of polymerized phantom membranes. Phys. Rev. E. 79, 040101(R).
Lai, Kang, Zhang, Wei-Bing, Zhou, Fa, Zeng, Fan, Tang, Bi-Yu, 2016. Bending rigidity of transition metal dichalcogenide monolayers from first-principles. J. Phys. D Appl. Phys. 49 (18), 185301.
Landau, L.D., Lifshitz, E.M., 1970. Theory of Elasticity, second ed. Pergamon Press, New York.
Le Doussal, P., Radzihovsky, L., 1992. Self-consistent theory of polymerized membranes. Phys. Rev. Lett. 69, 1209–1212.
Le Doussal, P., Radzihovsky, L., 1993. Flat glassy phases and wrinkling of polymerized membranes with long-range disorder. Phys. Rev. B 48, 3548–3551.
Le Doussal, Pierre, Radzihovsky, Leo, 2018. Anomalous elasticity, fluctuations and disorder in elastic membranes. Ann. Phys. 392, 340–410.
Lee, C., Wei, X., Kysar, J.W., Hone, J., 2008. Measurement of the elastic properties and intrinsic strength of monolayer graphene. Science 321 (385).
Leong, T.G., Randall, C.L., Benson, B.R., Bassik, N., Stern, G.M., Gracias, D.H., 2015. Tetherless thermobiochemically actuated microgrippers. Proc. Natl. Acad. Sci. USA 106, 703–708.
Liang, Xiaojun, Purohit, Prashant K., 2016. A fluctuating elastic plate and a cell model for lipid membranes. J. Mech. Phys. Solids 90, 29–44.
Lindemann, F.A., 1910. Über die berechnung molekularer eigenfrequenzen. Physik. Zeits. 11, 609–612.
Los, J.H., Fasolino, A., Katsnelson, M.I., 2016. Scaling behavior and strain dependence of in-plane elastic properties of graphene. Phys. Rev. Lett. 116, 015901.
Los, J.H., Katsnelson, M.I., Yazyev, O.V., Zakharchenko, K.V., Fasolino, A., 2009. Scaling properties of flexible membranes from atomistic simulations: Application to graphene. Phys. Rev. B 80, 121405(R).
Malachowski, K., Jamal, M., Jin, Q., Polat, B., Morris, C.J., Gracias, D.H., 2014. Self-folding single cell grippers. Nano Lett. 14, 4164–4170.
Mariani, Eros, von Oppen, Felix, 2008. Flexural phonons in free-standing graphene. Phys. Rev. Lett. 100, 076801.
Mariani, Eros, von Oppen, Felix, 2010. Temperature-dependent resistivity of suspended graphene. Phys. Rev. B 82, 195403.
Miskin, Marc Z., Dorsey, Kyle J., Bircan, Baris, Han, Yimo, Muller, David A., McEuen, Paul L., Cohen, Itai, 2018. Graphene-based bimorphs for micron-sized, autonomous origami machines. Proc. Natl. Acad. Sci. USA 115 (3), 466–470.
Morse, D.C., Lubensky, T.C., 1992. Curvature disorder in tethered membranes: A new flat phase at t=0. Phys. Rev. A. 46, 1751–1768.
Nagashima, S., Ha, H.D., Kim, D.H., Košmrlj, A., Stone, H.A., Moon, M.-W., 2017. Spontaneous formation of aligned DNA nanowires by capillarity-induced skin folding. Proc. Natl. Acad. Sci. USA 114, 6233–6237.
Nelson, D.R., Peliti, L., 1987. Fluctuations in membranes with crystalline and hexatic order. J. Phys. (France) 48 (1085).
Nelson, D.R., Piran, T., Weinberg, S. (Eds.), 2004. Statistical Mechanics of Membranes and Surfaces, second ed. World Scientific, Singapore.
Nelson, D.R., Radzihovsky, L., 1991. Polymerized membranes with quenched random internal disorder. Europhys. Lett. 16, 79–84.
Novozhilov, V.V., 1959. The Theory of Thin Shells.. Noordhoff, Gronigen.
Park, Y., Best, C.A., Badizadegan, K., Dasari, R.R., Feld, M.S., Kuriabova, T., Henle, M.L., Levine, A.J., Popescu, G., 2010. Measurement of red blood cell mechanics during morphological changes. Proc. Natl. Acad. Sci. USA 107, 6731–6736.
Paulose, J., Vliegenthart, G.A., Gompper, G., Nelson, D.R., 2012. Fluctuating shells under pressure. Proc. Natl. Acad. Sci. USA 109, 19551–19556.
Paulsen, J.D., Hohlfeld, E., King, H., Huang, J., Qiu, Z., Russell, T.P., Menon, N., Vella, D., Davidovitch, B., 2016. Curvature-induced stiffness and the spatial variation of wavelength in wrinkled sheets. Proc. Natl. Acad. Sci. USA 113, 1144–1149.
Plimpton, Steve, 1995. Fast parallel algorithms for short-range molecular dynamics. J. Comput. Phys. 117 (1), 1–19.
Ploehn, Harry J., Liu, Chunyan, 2006. Quantitative analysis of montmorillonite platelet size by atomic force microscopy. Ind. Eng. Chem. Res 45 (21), 7025–7034.
Radzihovsky, L., Nelson, D.R., 1991. Statistical-mechanics of randomly polymerized membranes. Phys. Rev. A. 44, 3525–3542.
Radzihovsky, Leo, Toner, J., 1998. Elasticity, shape fluctuations, and phase transitions in the new tubule phase of anisotropic tethered membranes. Phys. Rev. E 57, 1832–1863.
Reynolds, Michael F., McGill, Kathryn L., Wang, Maritha A., Gao, Hui, Mujid, Fauzia, Kang, Kibum, Park, Jiwoong, Miskin, Marc Z., Cohen, Itai, McEuen, Paul L., 2019. Capillary origami with atomically thin membranes. Nano Lett. 19 (9), 6221–6226.
Roldan, R., Fasolino, A., Zakharchenko, K.V., Katsnelson, M.I., 2011. Suppression of anharmonicities in crystalline membranes by external strain. Phys. Rev. B. 83, 174104.
Ruiz-García, M., Bonilla, L.L., Prados, A., 2015. Ripples in hexagonal lattices of atoms coupled to glauber spins. J. Stat. Mech. Theory Exp. 2015 (5), P05015.
Ruiz-García, Miguel, Bonilla, Luis L., Prados, Antonio, 2016. STM-driven transition from rippled to buckled graphene in a spin-membrane model. Phys. Rev. B 94 (20), 205404.
Ruiz-Garcia, M., Bonilla, L.L., Prados, A., 2017. Bifurcation analysis and phase diagram of a spin-string model with buckled states. Phys. Rev. E 96 (6), 062147.
Russell, Emily R., Sknepnek, Rastko, Bowick, Mark, 2017. Stiffening thermal membranes by cutting. Phys. Rev. E 96, 013002.
San-Jose, P., González, J., Guinea, F., 2011. Electron-induced rippling in graphene. Phys. Rev. Lett. 106, 045502.
Schmidt, B., Fraternali, F., 2012. Universal formulae for the limiting elastic energy of membrane networks. J. Mech. Phys. Solids 60, 172–180.
Seung, H.S., Nelson, D.R., 1988. Defects in flexible membranes with crystalline order. Phys. Rev. A 38, 1005–1018.
Singh, A.R., Košmrlj, A., Bruinsma, R., 2020. Finite temperature phase behavior of viral capsids as oriented particle shells. Phys. Rev. Lett. 124 (15), 158101.
Stoop, N., Lagrange, R., Terwagne, D., Reis, P.M., Dunkel, J., 2015. Curvature-induced symmetry breaking determines elastic surface patterns. Nature Mater. 14, 337–342.
Suter, James L., Coveney, Peter V., Chris, Greenwell H., Thyveetil, Mary-Ann, 2007. Large-scale molecular dynamics study of montmorillonite clay: emergence of undulatory fluctuations and determination of material properties. J. Phys. Chem. C 111 (23), 8248–8259.
Timoshenko, S.P., 1953. History of Strength of Materials. McGraw-Hill, New York.
Timoshenko, S., Woinowsky-Krieger, S., 1959. Theory of Plates and Shells, 2nd Edn. McGraw-Hill, New York.
Toner, John, 1989. Elastic anisotropies and long-ranged interactions in solid membranes. Phys. Rev. Lett. 62 (8), 905.
Tröster, A., 2013. High-precision fourier Monte Carlo simulation of crystalline membranes. Phys. Rev. B 87, 104112.
Tröster, A., 2015. Fourier Monte Carlo renormalization-group approach to crystalline membranes. Phys. Rev. E 91, 022132.
Tuckerman, Mark, 2010. Statistical Mechanics: Theory and Molecular Simulation. Oxford University Press.
Turlier, H., Fedosov, D.A., Audoly, B., Auth, T., Gov, N.S., Sykes, C., Joanny, J.-F., Gompper, G., Betz, T., 2016. Equilibrium physics breakdown reveals the active nature of red blood cell flickering. Nat. Phys. 12, 513–519.
van der Heijden, A.M.A., 2009. W. T. Koiter's Elastic Stability of Solids and Structures. Cambridge University Press, New York.
Wan, Duanduan, Nelson, David R., Bowick, Mark J., 2017. Thermal stiffening of clamped elastic ribbons. Phys. Rev. B 96, 014106.
Waugh, R., Evans, E.A., 1979. Thermoelasticity of red blood cell membrane. Biophys. J. 26, 115–131.
Xu, Weinan, Qin, Zhao, Chen, Chun-Teh, Kwag, Hye Rin, Ma, Qinli, Sarkar, Anjishnu, Buehler Markus, J., Gracias, David H., 2017. Ultrathin thermoresponsive self-folding 3D graphene. Sci. Adv. 3 (10), e1701084.
Zhang, Z., Davis, H.T., Kroll, D.M., 1993. Scaling behavior of self-avoiding tethered vesicles. Phys. Rev. E 48, R651–R654.
Zhang, Y., Yan, Z., Nan, K., Xiao, D., Liu, Y., Luan, H., Fue, H., Wang, X., Yang, Q., Wang, J., Ren, W., Si, H., Liu, F., Yang, L., Li, H., Wang, J., Guo, X., Luo, H., Wang, L., Huang, Y., Rogers, J.A., 2015. A mechanically driven form of kirigami as a route to 3D mesostructures in micro/nanomembranes. Proc. Natl. Acad. Sci. USA 112, 11757–11764.